Calculating Reynolds Stresses from ADCP Measurements in the Presence of Surface Gravity Waves Using the Cospectra-Fit Method

ANTHONY R. KIRINCICH AND STEVEN J. LENTZ

Woods Hole Oceanographic Institution, Woods Hole, Massachusetts

GREGORY P. GERBI

Rutgers, The State University of New Jersey, New Brunswick, New Jersey

ABSTRACT

Recently, the velocity observations of acoustic Doppler current profilers (ADCPs) have been successfully used to estimate turbulent Reynolds stresses in estuaries and tidal channels. However, the presence of surface gravity waves can significantly bias stress estimates, limiting application of the technique in the coastal ocean. This work describes a new approach to estimate Reynolds stresses from ADCP velocities obtained in the presence of waves. The method fits an established semiempirical model of boundary layer turbulence to the measured turbulent cospectra at frequencies below those of surface gravity waves to estimate the stress. Applied to ADCP observations made in weakly stratified waters and variable significant wave heights, estimated near-bottom and near-surface stresses using this method compared well with independent estimates of the boundary stresses in contrast to previous methods. Additionally, the vertical structure of tidal stress estimated using the new approach matched that inferred from a linear momentum balance at stress levels below the estimated stress uncertainties. Because the method makes an estimate of the horizontal turbulent length scales present as part of the model fit, these results can also enable a direct correction for the mean bias errors resulting from instrument tilt, if these scales are long relative to the beam separation.

1. Introduction

Turbulent eddies play a critical role in most environmental fluid flows. The turbulent transfer of momentum by these eddies modifies lower-frequency, larger-scale velocity fluctuations by transferring boundary forces through the water column. Knowledge of these momentum fluxes, often described in a bulk sense as Reynolds stresses, are critical to studies of both boundary layer dynamics and stratified flows. This is especially true on the inner continental shelf of the coastal ocean where, with water depths of 10–50 m, the turbulent surface and bottom boundary layers often overlap and interact. Thus, the Reynolds stresses within these boundary layers, which can be altered by variable forcing and stratification, often control inner-shelf coastal circulation. Numerous inner-shelf studies (Lentz 1994; Munchow and Chant 2000; Garvine 2004) have demonstrated that vertical profiles of Reynolds stresses, typically parameterized using an eddy viscosity, are critical to better understand the mechanisms of exchange across the inner shelf.

Recent progress has been made in our ability to estimate Reynolds stresses using the in situ velocity observations of acoustic Doppler current profilers (ADCPs). Vertical profiles of Reynolds stresses have been successfully estimated from short (10–20 min) bursts of high-frequency (1–2-Hz sample rate) along-beam velocity (Stacey et al. 1999a,b; Rippeth et al. 2003; Williams and Simpson 2004). However, surface gravity waves dominate the energy spectrum of these short bursts in most coastal ocean environments, with wave orbital velocities being orders of magnitude larger than those of turbulent eddies. Thus, small but unavoidable errors in instrument orientation can result in wave-induced stress errors much larger than the Reynolds stresses themselves (Trowbridge 1998). As a result, much of the successful application of this method has been limited to tidal channels, rivers, or estuaries where wave orbital velocities were assumed to be smaller than turbulent velocities. Attempts to remove

Corresponding author address: Anthony R. Kirincich, Woods Hole Oceanographic Institution, 266 Woods Hole Road, Woods Hole, MA 02543.
E-mail: akirincich@whoi.edu

the wave biases in ADCP-based stress estimates obtained in the presence of surface gravity waves have had some success in mild wave climates (Whipple et al. 2006; Rosman et al. 2008). However, these methods appear unable to attain viable stress estimates during larger wave climates, as will be shown later.

It is important to note that, although ADCPs are not the ideal instrument for measuring turbulent fluctuations (Stacey et al. 1999a), they are one of the most commonly used profiling current meters in the coastal ocean. Thus, a method to accurately estimate Reynolds stresses in the presence of waves using this instrument would enable the regular collection of stress profiles that span the water column over shelves, greatly aiding our efforts to understand and model the dynamics of coastal flows. Routine estimates of Reynolds stresses in these flows would also help evaluate the turbulence closure methods used in coastal ocean numerical models, one of the largest sources of model uncertainty (Warner et al. 2005).

This paper describes and tests a new method, adapted from Gerbi et al. (2008) and referred to here as the cospectra-fit (CF) method, for estimating Reynolds stresses in the presence of surface gravity waves using ADCP-based velocity observations. As will be shown, applying the CF method to ADCP along-beam velocities obtained in the presence of waves provides useful estimates of Reynolds stresses in the coastal ocean, meaning wave-induced stress errors are small enough to yield accurate stress estimates in comparison with independent bottom stress, wind stress, and tidal stress estimates. The CF method also provides an estimate of the horizontal length scale of the dominant stress-carrying eddies, useful in assessing the anisotropy of the flow and accounting for stress errors resulting from instrument tilt. The observations utilized in this study are introduced first (section 2), followed by a description of ADCP-based stress-estimation methods (section 3) and a review of previous wave-bias removal techniques (section 4). The cospectra-fit method and its application to the test dataset are then described (section 5), and estimated stresses and tilt-related biases are evaluated (sections 6 and 7). Finally, differences between the CF and previous methods as well as potential limitations of the method are discussed (section 8), and conclusions are summarized (section 9).

2. The MVCO dataset

Velocity observations collected at the Martha's Vineyard Coastal Observatory (MVCO; available online at http://mvcodata.whoi.edu) are used as a test dataset for this study. Located in the inner shelf south of Martha's
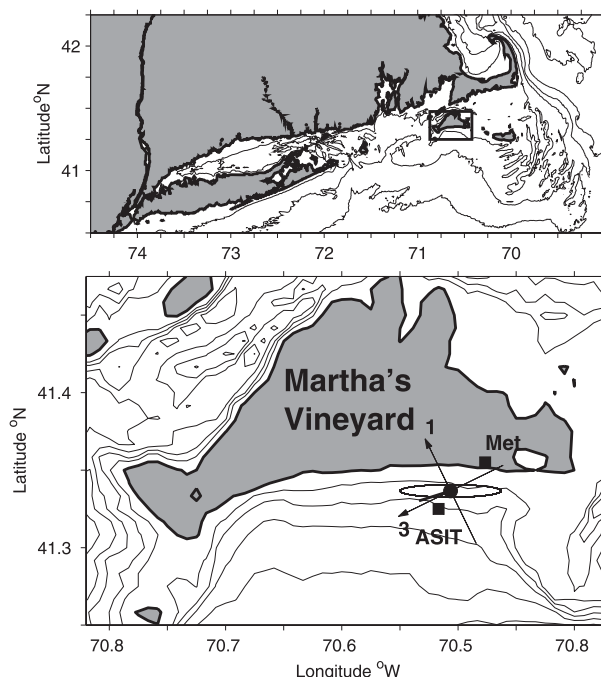

FIG. 1. Located in (top) the coastal waters south of Cape Cod, the MVCO underwater node is in 12 m of water (bottom) 1 km south of the island of Martha's Vineyard. The instrument-coordinate system used here (arrows 1 and 3, denoting the orientation of the ADCP beams) is shown at the site location (filled circle). For the study period, January 2008, the tidal ellipse of the M_2 tide (black ellipse) was oriented along isobaths, whereas the mean velocity vector (thick line; shown $\times$ 10) was oriented to the west-southwest.

Vineyard, Massachusetts (Fig. 1), MVCO's underwater node in 12 m of water supports an ADCP that has been collecting water velocities semicontinuously since 2001. The instrument, a 1200-kHz Teledyne RD Instruments (RDI) Workhorse Monitor, samples velocity profiles at 2 Hz using RDI water profiling mode 1 in continuous 20-min bursts for 9–16 (tide dependent) 0.5-m bins starting 3.3 m above the bottom.

A 30-day portion (1–30 January 2008) of the ADCP record was isolated to assess the performance of current ADCP-based stress-estimation methods and the viability of the cospectra-fit method. The timing and duration of the study period was chosen to minimize the potential for reduced turbulent length scales resulting from stratification effects—weak stratification is typically found at MVCO during winter months—and to encompass a number of wind and wave forcing events. Although recent studies (Williams and Simpson 2004; Nidzieko et al. 2006) have found that lower-noise floors and improved stress estimates are possible using RDI's faster-sampling mode 12, the mode-1 observations from MVCO are utilized here to investigate the possibility of stress estimates for this multiyear time series. During the 30-day

period, the ADCP was oriented with beam 3 (defined as the positive y axis) pointing toward 244°T (Fig. 1) with an instrument-measured pitch and roll of 2.3° and 3.4°, respectively. For simplicity, we use the instrument-coordinate system throughout this work, where u is the horizontal velocity in a plane defined by beams 1 and 2 (positive toward beam 1), v is the horizontal velocity in a plane defined by beams 3 and 4 (positive toward beam 3), and w is the vertical axis (positive upward from the instrument).

Conditions during the study period were marked by variable wind and wave forcing, as well as by strong tidal forcing. Wind velocities were measured nearby at MVCO's Air–Sea Interaction Tower (ASIT), which is located 1.2 km to the south-southwest in 17 m of water, and the Shore Meteorological Station, which is located 3 km to the north-northeast along the south coast of Martha's Vineyard (Fig. 1). Winds measured offshore at the ASIT, available after day 16, were highly correlated with but slightly larger in magnitude than shore-based winds (Fig. 2). Wind stresses were estimated following Large and Pond (1981), assuming neutral stability and rotated into the coordinate system defined by the ADCP. Wind stress varied greatly during the month, having a mean and peak stress of 0.12 and 0.55 Pa, but tidal forcing accounted for the largest source of burst-mean velocity variability (Fig. 2). The estimated M_2 tidal ellipse was orientated along isobaths (Fig. 1), whereas the depth-averaged mean velocity ($\times 10$, as shown in Fig. 1) was orientated to the west-southwest. The magnitudes of both were predominantly captured by velocity measurements along the 3–4 axis. Surface gravity waves generally approached Martha's Vineyard from the south (196°T)—aligned more with the 1–2 axis—with median wave heights and wave periods of 1.05 m and 5.7 s and standard deviations of 0.7 m and 2.2 s (Fig. 2).

To apply the CF method to ADCP velocities (section 4), spectra were computed from the raw along-beam velocity observations after careful screening for data quality. For each 20-min burst of 2-Hz velocities, data at each depth level were screened and flagged for bad data characteristics, which are defined by raw along-beam velocities greater than 2 m s^{-1}, beam correlations (a measure of velocity precision) less than 90 counts, and beam intensities less then 60 counts. Velocities in all beams from a flagged bin were removed and linearly interpolated over. Interpolations of 5 consecutive points (2.5 s of data) or more were rejected, and only continuous records longer than 1200 pings (10 min), in which the fraction of interpolated pings was less than 10%, were kept. Power spectra of the along-beam velocities ($S_{u_i u_i}$, where i is the beam number) were computed after detrending and tapering each 20-min burst time series

using a single Hanning window to reduce spectral noise while maximizing spectral resolution (Fig. 5). Variations to these methods were attempted, including using windowed, overlapping spectral estimates and ensemble averaging the raw ping data to 0.5-Hz temporal resolution for both 10- and 20-min bursts. All methods produced quantitatively similar results, in terms of model fit correlations and stress magnitudes; thus, the simplest method is used here.

3. ADCP-based stress-estimation methods

Horizontal Reynolds stresses are estimated from ADCP observations using the variance method. Adapted from atmospheric studies by Lohrmann et al. (1990) using pulse-to-pulse coherent sonar and first applied to Teledyne RDI ADCPs by Stacey et al. (1999a), this method uses the along-beam velocities from a four-beam ADCP in the Janus configuration to compute profiles of vertical Reynolds stress in the two horizontal directions. For an upward-looking instrument, where beams 1 and 2 are oriented along the roll axis of the instrument (the x axis) and beams 3 and 4 are oriented along the pitch axis of the instrument (the y axis), along-beam velocities in a given vertical bin can be written as

$$u_1 = -u \sin\theta - w \cos\theta, \tag{1}$$

$$u_2 = u \sin\theta - w \cos\theta, \tag{2}$$

$$u_3 = -v \sin\theta - w \cos\theta, \quad \text{and} \tag{3}$$

$$u_4 = v \sin\theta - w \cos\theta. \tag{4}$$

Here, u_1, u_2, u_3, and u_4 are along-beam velocities in each of the four beams; u, v, and w are the x, y, and z velocities in a right-handed coordinate system aligned with a plane defined by beams 1 and 2 (the 1–2 axis), and $\theta = 20°$ is the angle of the beams away from vertical. Thus, x and u are positive toward beam 1, y and v are positive toward beam 3, and z and w are positive upward. Using the Reynolds decomposition, written for the 1–2 axis as

$$u = U + \tilde{u} + u', \tag{5}$$

the total velocity u can be divided into mean $U = \overline{u}$ (where the overbar denotes time averaging), wave $\tilde{u}$, and turbulent u' components. If all fluctuations in a short (10–20 min) burst around a mean velocity are due to turbulent motions only, $\tilde{u} = 0$ in (5) and turbulence statistics are horizontally homogeneous, taking the variance of the along-beam velocity in Eqs. (1)–(4)
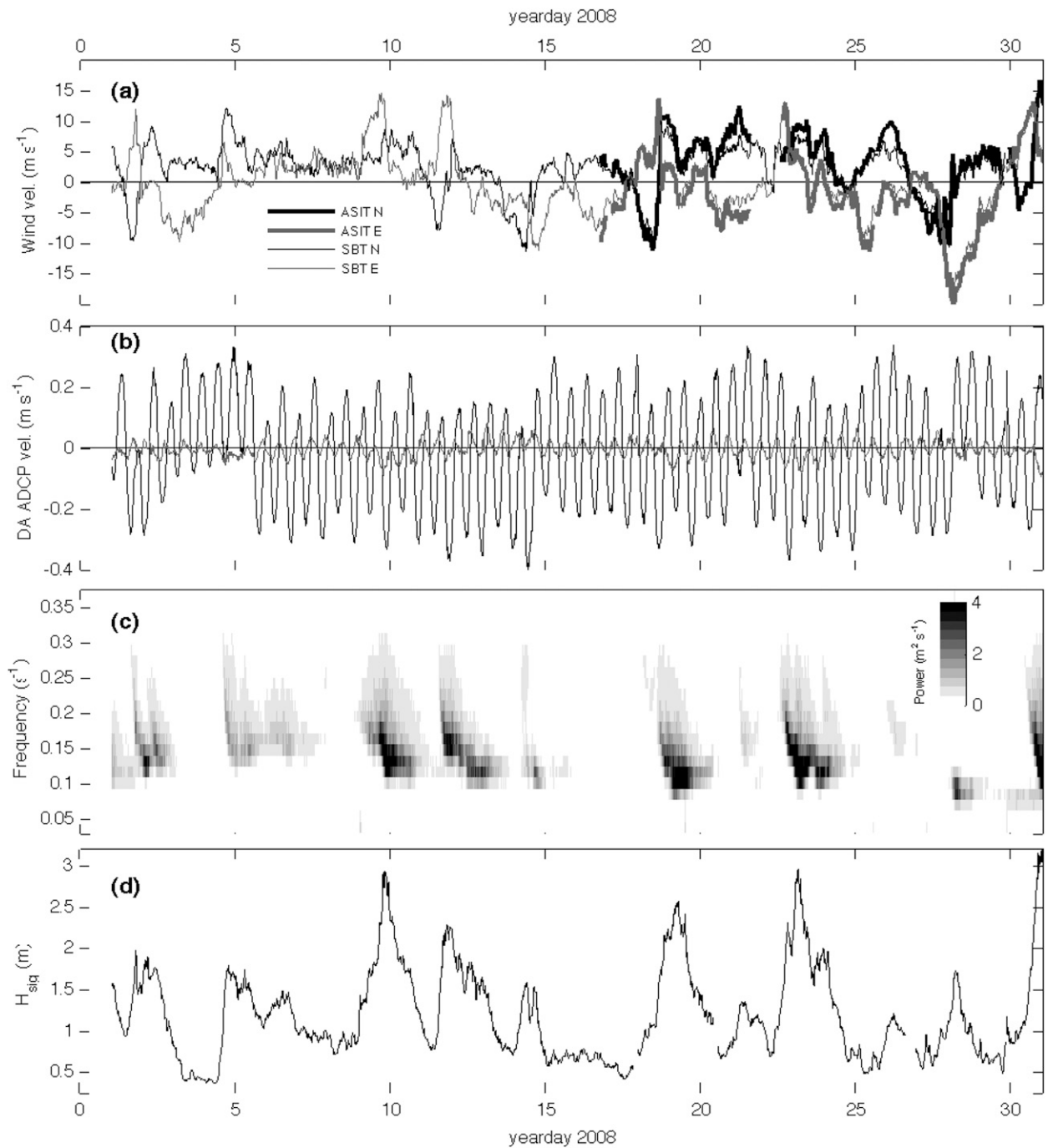
FIG. 2. Conditions for the study period: (a) available wind velocities at the shore-based tower (SBT) and ASIT; (b) depth-averaged east (black) and north (gray) water velocities from the MVCO 12-m ADCP; (c) frequency distribution of wave energy at MVCO; and (d) significant wave height at MVCO.

and subtracting equations of opposing beams leads to expressions for Reynolds stresses in the x, y, and z coordinate system,

$$\overline{u'w'} = \frac{\overline{u}_1^2 - \overline{u}_2^2}{4\cos\theta\sin\theta} \quad \text{and} \quad (6)$$

$$\overline{v'w'} = \frac{\overline{u}_3^2 - \overline{u}_4^2}{4\cos\theta\sin\theta}. \quad (7)$$

However, if the instrument is tilted relative to the x, y, and z coordinate system, additional terms exist. Given

small ($\sin\phi \sim \phi$) pitch (ϕ_p) and roll (ϕ_r) radian angles, (6) and (7) become

$$\overline{u'w'} = \frac{\overline{u_1^2} - \overline{u_2^2}}{4\cos\theta\sin\theta} + \phi_r(\overline{w'^2} - \overline{u'^2}) + \phi_p\frac{\overline{u'v'}}{\cos\theta} \quad \text{and} \tag{8}$$

$$\overline{v'w'} = \frac{\overline{u_3^2} - \overline{u_4^2}}{4\cos\theta\sin\theta} - \phi_p(\overline{w'^2} - \overline{v'^2}) - \phi_r\frac{\overline{u'v'}}{\cos\theta}. \tag{9}$$

Although the stress bias caused by the difference of the horizontal and vertical velocity variances—term 3 in (8) and (9)—would be zero for isotropic turbulence ($\overline{w'^2} = \overline{u'^2} = \overline{v'^2}$), because of the anisotropy usually present, this term can be large in comparison to the true stress. In contrast, the covariance of the horizontal velocities—term 4 in (8) and (9)—is thought to be small (Lu and Lueck 1999).

Multiple studies have used stresses estimated from (6) and (7) to examine the dynamics of tidal channels and estuaries with good success (Stacey et al. 1999a; Rippeth et al. 2003; Williams and Simpson 2004; Nidzieko et al. 2006). Uncertainty estimates for variance-method stresses have been developed by Stacey et al. (1999a), Lu and Lueck (1999), and Williams and Simpson (2004). Further comparisons between variance-method stresses and microstructure-based dissipation measurements have shown good agreement (Rippeth et al. 2002, 2003).

Application of the variance method is predominantly limited by two sources of error that can greatly bias the estimated stress. The instrument will average all turbulent fluctuations with length scales less than twice the vertical bin thickness. Thus, the variance method is likely to underestimate stresses in more stratified conditions when the vertical scale of the dominant stress-carrying eddies might be smaller than the bin thickness (Stacey et al. 1999a; Williams and Simpson 2004). Surface gravity waves, however, provide the largest source of error in most coastal ocean environments. According to linear wave theory, the horizontal and vertical velocities of irrotational waves should be uncorrelated and thus cause no contribution to the stress. However, the orbital velocities associated with waves are typically orders of magnitude larger than the turbulent velocities of interest. Thus, imperfect knowledge of instrument orientation, the presence of sloping bottoms, or nonlinear effects can lead to an apparent covariance between horizontal and vertical wave velocities (Trowbridge 1998). These wave-induced stress errors are small relative to the orbital velocity variances themselves but can be equal to or greater than the Reynolds stresses of interest. A formal derivation of the effect of these wave-induced biases on the true stresses has been given by Trowbridge (1998).

4. Previous wave-bias removal methods

Recent studies of oceanic turbulence using acoustic Doppler velocimeters (ADVs) have attempted to reduce wave-induced stress errors by differencing velocities measured at two horizontally or vertically separated sensors. These methods rely on the assumption that wave velocities are correlated (Trowbridge 1998) or coherent (Shaw and Trowbridge 2001) over the separation distance but that turbulent velocities are not. Reynolds stresses are estimated from the covariance of the differenced or filtered velocities. Using arrays of ADVs, these methods have had some success representing turbulent stresses within the surf zone (Trowbridge and Elgar 2001, 2003) and the outer-shelf bottom boundary layer (Shaw and Trowbridge 2001) but do poorly in the presence of stronger waves and weaker stresses (Feddersen and Williams 2007) as well as more complex wave climates (Gerbi et al. 2008).

The techniques of Trowbridge (1998) and Shaw and Trowbridge (2001) were adapted for ADCP-based observations by Whipple et al. (2006) and Rosman et al. (2008), respectively. Whipple et al. (2006) differenced vertically separated along-beam velocities, using linear wave theory to account for vertical decay of wave velocities with depth, before applying the variance method. With observations from an estuary 8 m deep, estimated stresses were similar in magnitude to the wind and bottom stress during weak winds and small wave conditions but became biased during moderate wind speeds and wave heights (Whipple et al. 2006). Rosman et al. (2008) examined three different wave velocity removal methods: variance differencing (Whipple et al. 2006), vertical (along beam) adaptive filtering (AF; Shaw and Trowbridge 2001), and horizontal (beam-to-beam) AF. Applying these techniques to inner-shelf ADCP observations, the vertical AF method appeared to have the smallest wave-induced stress biases (Rosman et al. 2008), although correlations between AF-method stress estimates for the bottommost bin and a quadratic drag law based on the burst-mean horizontal velocities of the same bin were similar for both the variance differencing and AF methods. Similar to that seen for the ADV-based stress studies, wave-induced biases were lowest during longer-period, narrowbanded waves; however, both methods became less accurate for increased wave heights, decreased wave periods, and locations closer to the surface (Rosman et al. 2008).

We evaluated the AF method's performance for the MVCO ADCP dataset using MATLAB-based code provided by J. Rosman (2009, personal communication). As described in detail by Shaw and Trowbridge (2001) and Rosman et al. (2008), the method uses least
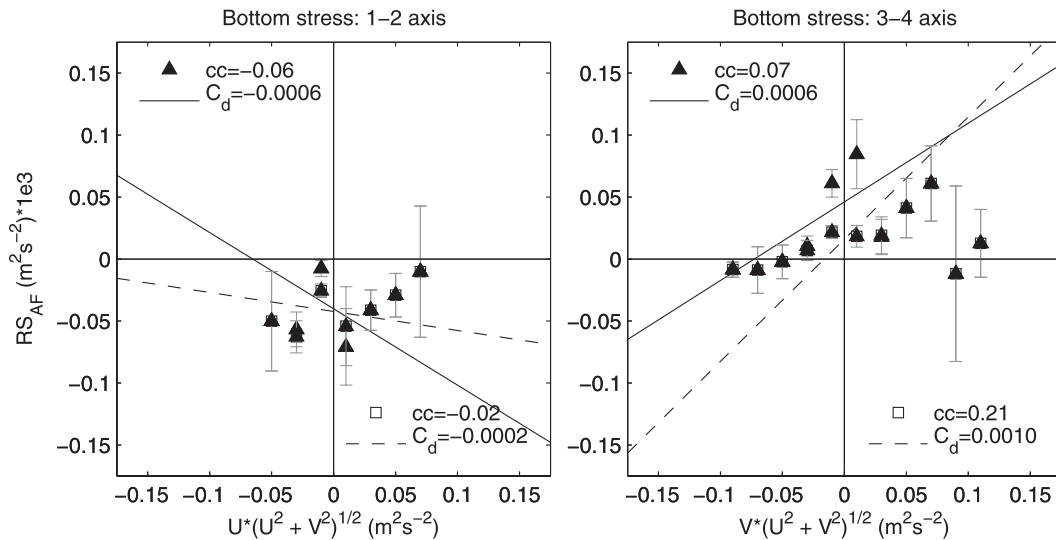
FIG. 3. Bin-averaged comparisons of the bin-1 AF-method Reynolds stress estimates to the quadratic drag law, calculated using burst-mean velocities from the same depth bin. AF-method stress estimates were calculated for the dataset following Rosman et al. (2008). For the (left) 1–2 and (right) 3–4 axes, bin-averaged bottom stresses are shown for all data (triangles) and only bursts meeting both CF-method criteria (squares). Standard error bounds, estimated using the effective degrees of freedom (Chelton 1983), are given for each bin. Linear regressions, slopes, and CC between time series of all AF-method stress estimates (dashed line; C_d) or only those bursts meeting the CF-method criteria (solid line; C_d) vs quadratic drag law are shown.

squares filtering to estimate the part of the velocity at one along-beam location ($u_i^{(1)}$, where i is the beam number) that is coherent with the velocity at a second along-beam location ($u_i^{(2)}$). As discussed earlier, the velocity coherent between locations is assumed to be wave velocities. Filter weights h are determined by the matrix equation,

$$h = (\mathbf{A}^{\mathrm{T}}\mathbf{A})^{-1}\mathbf{A}^{\mathrm{T}}u_i^{(1)}, \qquad (10)$$

where $\mathbf{A}$ is an $M \times N$ windowed data matrix of $u_i^{(2)}$ velocities, M is the length of the $u_i^{(2)}$ time series, and N ($= 11$ here) is the number of filter weights. The estimated wave-induced velocities in $u_i^{(1)}$ are then

$$\tilde{u}_i^{(1)} = \mathbf{A}h, \qquad (11)$$

leading to a mean and turbulence only velocity of

$$\Delta u_i^{(1)} = u_i^{(1)} - \tilde{u}_i^{(1)} \qquad (12)$$

that is used in (6) and (7) to estimate Reynolds stresses. Similar to Rosman et al. (2008), a vertical separation distance of 3 m was chosen for the MVCO ADCP dataset based as this separation distance maximized the correlation between the depth-averaged AF-method stresses

and a quadratic drag law in the 3–4 direction. For the conditions present at MVCO, the AF-method near-bottom stresses compared poorly to estimates of the quadratic drag law ($\mathbf{U}|\mathbf{U}|$), calculated from the burst-mean horizontal 1–2 and 3–4 velocities. Correlations for these comparisons were near zero at −0.06 and 0.04 for the 1–2 and 3–4 axes, respectively. For both axes, bin averages of the estimated stress by the drag law (Fig. 3, triangles) showed no trends and had large standard errors. Additional comparisons of near-bottom stresses estimated using the velocity difference method (Whipple et al. 2006) were considerably worse than that described here for the AF method.

The mixed results of previous wave-bias removal methods reported in the literature, as well as the failure of these methods here, suggest that it is difficult to know the wave orbital velocities precisely enough for most coastal ocean wave climates to ensure that residual wave velocities are significantly less than the turbulent velocities of interest. Within the wave band, wave velocities are orders of magnitude greater than expected turbulent velocities. Thus, to use this part of the spectrum to calculate turbulent stresses directly from observations, wave velocities must be known to $O(10^{-4})\%$ to reduce residual wave velocities to levels significantly less then the turbulent velocities of interest (Trowbridge 1998). From the results described earlier for both ADV and ADCP observations, differencing or filtering methods

appear unable to reach this level of accuracy for more complex wave conditions. Additionally, these approaches assume a vertical turbulent length scale for differencing or filtering, which would ignore turbulent fluctuations with length scales longer than the differencing length and limit the overall vertical resolution of the estimated stress profiles from an ADCP.

5. The cospectra-fit method

Recently, Gerbi et al. (2008) used an alternative approach to successfully estimate unbiased Reynolds stresses from ADVs deployed 1–3 m below the surface during conditions where previous methods failed. Referred to here as the cospectra-fit (CF) method, this method works by only considering the velocity cospectrum at frequencies below those of surface gravity waves, and it fits a model to the observed cospectrum at these frequencies to estimate the total stress present. The theory behind the CF method is described first, followed by its adaptation to the ADCP-based velocities collected at MVCO.

a. Method background

The CF method assumes that a semiempirical model of the velocity cospectrum, based on observations of atmospheric boundary layer turbulence by Kaimel et al. (1972), appropriately describes the spectral shape of turbulent cospectral energy. Stated here for the $(x–z)$ plane, the one-sided model cospectrum is

$$\text{Co}^*_{uw}(k) = \overline{u'w'}^* \left(\frac{7}{3\pi} \sin \frac{3\pi}{7} \right) \frac{1/k_o}{1 + (k/k_o)^{7/3}}, \quad (13)$$

where model-derived stress and cospectra are denoted by an asterisk. The model turbulent cospectrum Co^*_{uw}, a function of wavenumber ($k = 2\pi/\lambda$; where λ is the wavelength), can be fully defined by two parameters: the total Reynolds stress, $\overline{u'w'}^*$ (the integral of the model cospectrum), and a "roll off" wavenumber (k_o; a measure of the dominant length scale of turbulent fluctuations). The model assumes constant power at low frequencies and rolls off at higher frequencies (Fig. 4a). Multiplying the model cospectrum by wavenumber k gives a variance-preserving cospectrum where k_o defines the peak of the model cospectrum (Fig. 4b). Additionally, the cumulative integral of the cospectrum (Fig. 4c)—the Ogive curve—increases with increasing wavenumber to a maximum value equal to the total Reynolds stress at the highest wavenumbers. Using Taylor's frozen-flow hypothesis, observed frequency cospectra from a point measurement of velocity can be related to the wavenumber cospectra of the model using the mean velocity
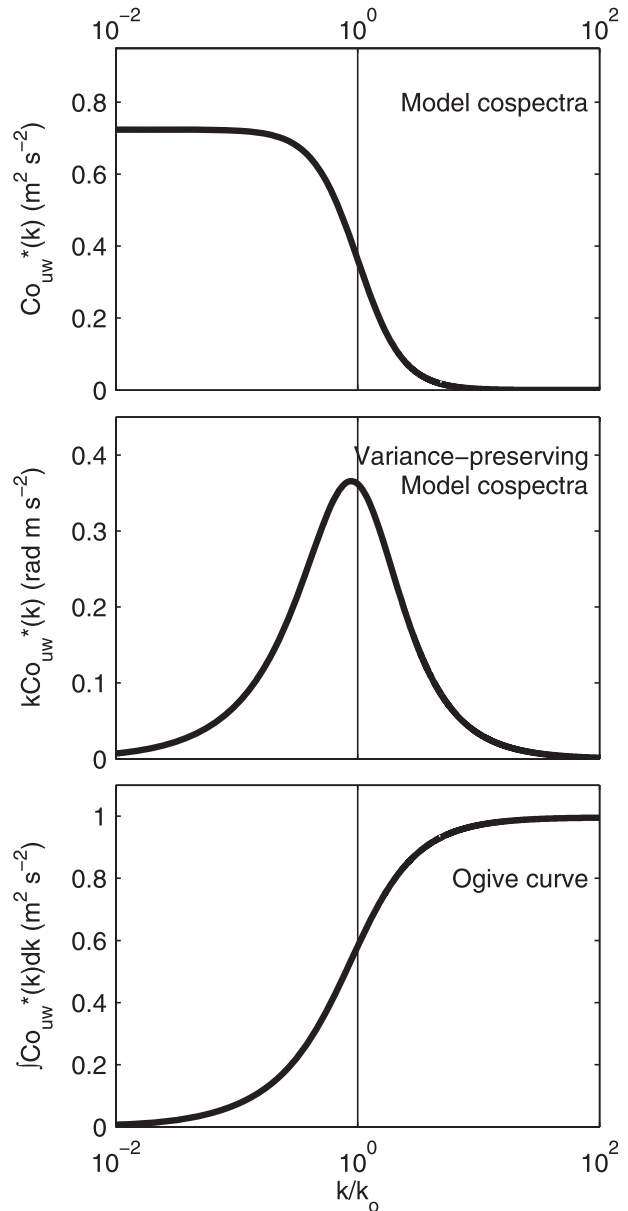

FIG. 4. The Kaimel et al. (1972) semiempirical model for boundary layer turbulence in both (top) cospectrum and (middle) variance-preserving cospectrum forms. The cumulative integral of the model cospectrum is (bottom) the Ogive curve.

of the burst as $\omega = k|\mathbf{U}|$. The CF method fits—in a least squares sense—the model cospectrum to the observed cospectrum at wavenumbers below those of surface gravity waves to derive wave-free estimates of $\overline{u'w'}^*$ and k_o.

A drawback of utilizing only the below–wave band cospectrum for a model fit dependent on the frozen-flow hypothesis is the potential for reduced stress estimates resulting from the aliasing of turbulent energy to frequencies

above those considered. The unsteady advection of turbulent eddies by surface wave velocities can alias lower-frequency turbulent energy into the wave band (Lumley and Terray 1983; Trowbridge and Elgar 2001; Gerbi et al. 2008), decreasing the total amount of turbulent energy seen below the wave band and thus reducing the magnitude of a Reynolds stress estimated via the model fit of the below–wave band cospectrum. Gerbi et al. (2008) developed a threshold criterion based on the ratio of the standard deviation of the wave orbital velocity (σ_{wave}) to the burst-mean (or drift) velocity ($U_d = |\mathbf{U}|$). Limiting the results to those where $\sigma_{\mathrm{wave}}/U_d \leq 2$ limits this bias to less than 15% of the total stress present.

b. Applying the CF method to ADCP velocities

Combining the basics of the variance method with this new approach developed by Gerbi et al. (2008), the along-beam velocities measured by an ADCP can be used to estimate turbulent Reynolds stresses in the presence of surface gravity waves. The variance method in (6) and (7) can be rewritten for one-sided velocity spectra as

$$\mathrm{Co}_{uw}(\omega) = \frac{S_{u_1 u_1}(\omega) - S_{u_2 u_2}(\omega)}{4\cos\theta\sin\theta} \quad (14)$$

$$\mathrm{Co}_{vw}(\omega) = \frac{S_{u_3 u_3}(\omega) - S_{u_4 u_4}(\omega)}{4\cos\theta\sin\theta}, \quad (15)$$

where the difference of velocity spectra $S_{u_i u_i}$ from opposing beams gives the observed cospectra (Co_{uw} and Co_{vw}) of horizontal and vertical velocities. The full-spectrum integrals of these cospectra, the covariances, are the Reynolds stresses ($\overline{u'w'}$ and $\overline{v'w'}$) computed in (6) and (7).

Stresses along both axes are estimated for each 20-min burst and depth bin of the MVCO dataset using (14) and (15) as follows: A wave band cutoff frequency ω_{wc} is defined by comparing the mean along-beam velocity spectrum $\overline{S_{u_i u_i}}$ with one for vertical velocity S_{ww}, derived from the spectrum of a collocated pressure sensor S_{pp} using linear wave theory:

$$S_{ww} = S_{pp} \frac{k^2}{\rho^2 \omega^2} \tanh^2 k(z+h). \quad (16)$$

Because energy from wave-induced motions of the sea surface are orders of magnitude larger than pressure fluctuations because of lower-frequency turbulence, this pressure-based vertical velocity spectrum serves as a reliable indicator of the wave band energy. The frequency

at which S_{ww} rises to 30% of $\overline{S_{u_i u_i}}$ was defined as the wave band cutoff frequency ω_{wc} (Fig. 5a). At frequencies higher than the wave band, S_{ww} increases because of sensor noise (Fig. 5a). Converting the cutoff frequency ω_{wc} to a wavenumber k_{wc} using $\omega = k|\mathbf{U}|$, cutoff wavenumbers decrease as the surface is approached (Fig. 6), ranging from a median of 3.8 rad m^{-1} (1.6 m wavelength) at 3.3 m above the bottom to a median of 2.2 rad m^{-1} (3 m wavelength) at 7.8 m above the bottom (4 m below the surface). By similarly converting the frequency cospectra [$\mathrm{Co}_{uw}(\omega)$ and $\mathrm{Co}_{vw}(\omega)$] to a wavenumber cospectra [$\mathrm{Co}_{uw}(k)$ and $\mathrm{Co}_{vw}(k)$], the total stresses are estimated by simple least squares fits between the Ogive curves—the cumulative integral—of the observed cospectra and the model cospectra (Fig. 5b) at wavenumbers below the cutoff wavenumber k_{wc}. Fitting the Ogive curves instead of the cospectra themselves reduces the effect of spectral noise and results in a mean variance-preserving cospectrum that more closely matched the model (Fig. 7).

Screening criteria were applied to ensure the quality of the model fit to the observations and the reduction of wave–drift bias to acceptable levels. Fits where k_o was outside of the observed wavenumber range ($k_o > k_{\mathrm{wc}}$ or $k_o < k_{\mathrm{min}}$) were rejected, limiting the data returns to 65% of the total possible bursts. Applying the wave/drift bias threshold, $\sigma_{\mathrm{wave}}/U_d \leq 2$, further limited the data return to 40% of the total possible bursts. Applying these criteria, viable stress estimates occurred more frequently in the lower part of the water column where wave velocities were reduced and not at all during large wave and weak current conditions. The roll-off wavenumber k_o was more likely to be higher than k_{wc} and was thus excluded when dominant surface gravity waves had long periods (small wavenumber) or when the dominant turbulent length scales ($\lambda_o = 2\pi/k_o$) were small. Median values for k_o, in the form of λ_o, are discussed in section 6d (and given in Fig. 12).

c. Evaluating the model fit

The skill of the Kaimel et al. (1972) model fit to the observations was assessed using two tests: a comparison of the observed below–wave band variance-preserving cospectrum to the theoretical model and a comparison of the model-estimated stress to the observed below–wave band covariance. To make the first comparison, the observed variance-preserving cospectra from all depths–bursts passing the threshold criteria were normalized by the model-estimated Reynolds stress and grouped into bins by wavenumber, normalized by the model-estimated roll-off wavenumber. Median values and bootstrapped standard error, utilized to reduce the effect of spectra noise, are shown for each wavenumber
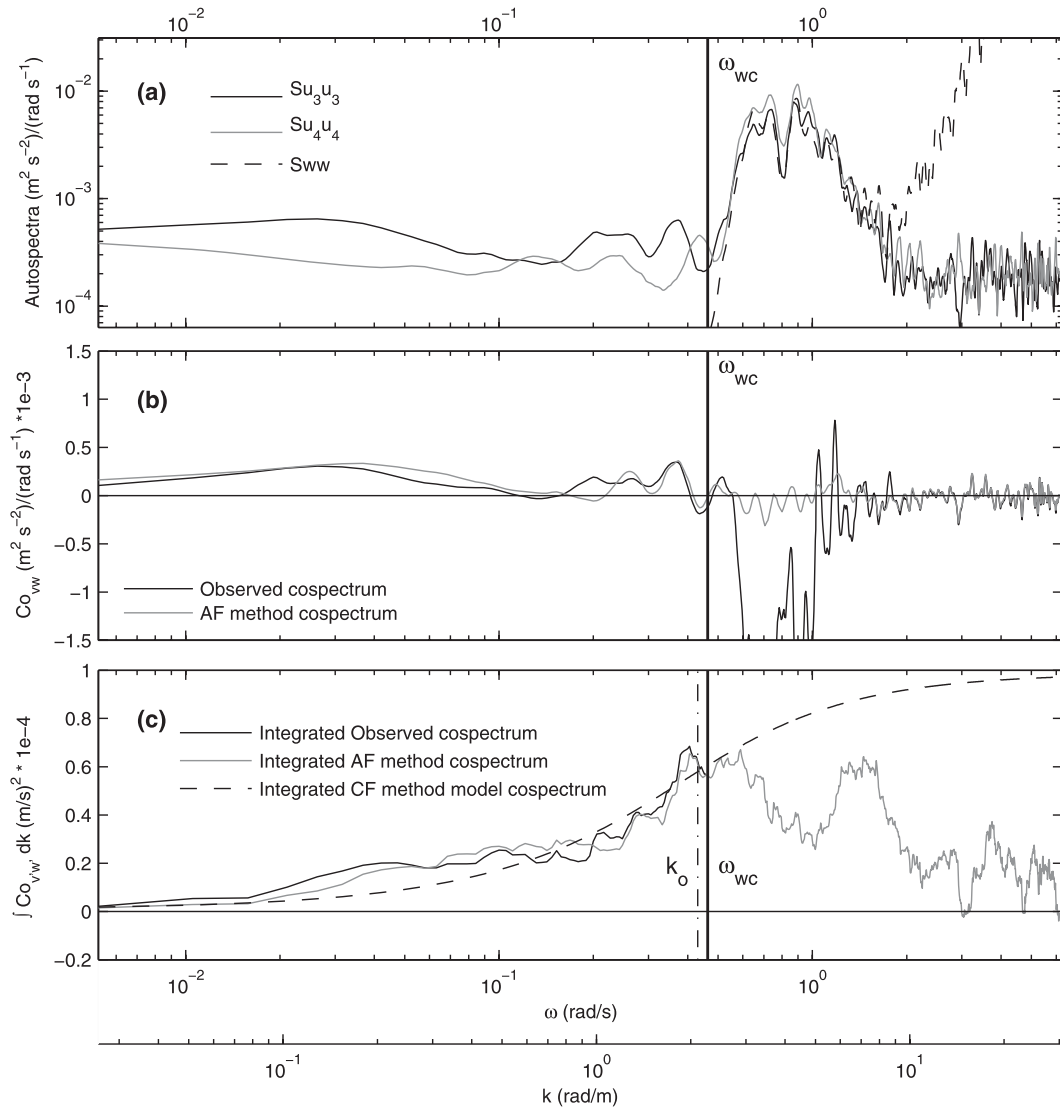
FIG. 5. Velocity spectra, cospectra, and integrated cospectra for a sample burst from the 3–4 axis at 3.8 m above the bottom at 0700 UTC 1 Jan: (a) along-beam velocity spectra for beams 3 (black line) and 4 (gray line) along with the pressure-based vertical velocity spectra (dashed line); (b) observed cospectra, estimated following Eqs. (14) and (15) using the raw velocity spectra (black line) and the filtered velocities defined by Eq. (12) for the AF method (gray line); and (c) integrated cospectra (Ogive curves) for the observed velocities (black line), AF method (gray line), and the model fit to the CF-method below–wave band cospectra (dashed line). Although raw cospectra are used in the model fit, all spectra were smoothed with a 9-point running mean to reduce spectral noise for display.

bin in Fig. 7. These estimates of the mean observed below–wave band cospectra fall close to the theoretical model cospectra, defined by (4). Observations correspond closely to the model at wavenumbers between $\log_{10}(k/k_o) = 0$ (i.e., $k = k_o$) and $\log_{10}(k/k_o) = 0.7$ but are slightly less than the model at wavenumbers less than k_o. This comparison is similar to that found by Gerbi et al. (2008) for ADV-based stress estimates using the CF method. For the second comparison, the total stresses (covariances) estimated by the model fit

to the data were highly correlated with and close in magnitude to the observed below–wave band covariances, the integral of the measured cospectra below the wave band cutoff (Fig. 8). Along both axes, correlation coefficients (CC) were close to 1 and linear regression slopes were near 1.15. With data return limited to bursts where $k_o > k_{wc}$, if the model used was appropriate, then most of the energy in the turbulence cospectrum should be captured by the below–wave band cospectrum.
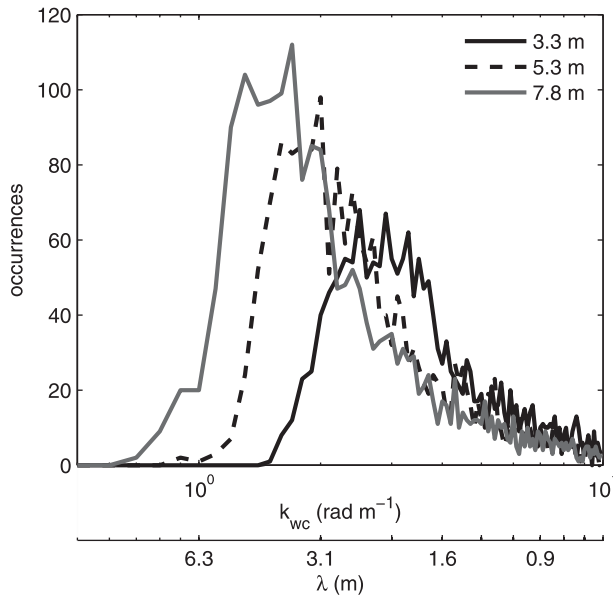
FIG. 6. Histograms of the wave band cutoff wavenumber ($k_{wc} = \omega_{wc}/|\mathbf{U}|$) for 3.3, 5.3, and 7.8 m above the bottom.

d. Uncertainty

We estimate the uncertainty of the below–wave band covariance, and by extension the total stress, using a nonparametric (Monte Carlo type) approach. Following Lu and Lueck (1999), (6) and (7) can be rewritten as a covariance of a sum and difference velocity at zero lag as

$$\overline{u'w'} = \frac{\overline{u_1'^2} - \overline{u_2'^2}}{4\cos\theta\sin\theta}$$
$$= \frac{1}{4\cos\theta\sin\theta}\left[\overline{(u_1' + u_2')(u_1' - u_2')}\right] \quad \text{and} \quad (17)$$

$$\overline{v'w'} = \frac{\overline{u_3'^2} - \overline{u_4'^2}}{4\cos\theta\sin\theta} = \frac{1}{4\cos\theta\sin\theta}\left[\overline{(u_3' + u_4')(u_3' - u_4')}\right].$$
$$(18)$$

For each burst, we shift (or lag) the sum or difference velocity time series many (1000) times by a random amount greater than the data-based decorrelation time scale (30 s) and compute the cospectrum and below–wave band covariance to build a histogram of lagged-covariance estimates. Confidence intervals then can be calculated for the observed covariance by considering these histograms to be probability density functions. However, the standard deviation σ of the histograms are presented here as the covariance, or stress, uncertainty for comparison with previous variance-method uncertainties. Uncertainties estimated via this method were functions of the below–wave band covariance (Fig. 9).
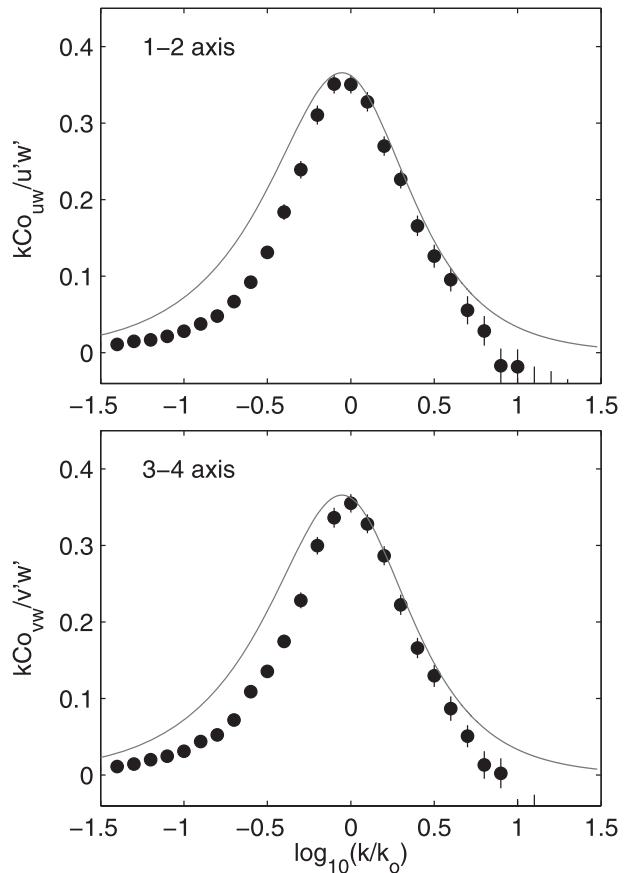

FIG. 7. Comparison of the observed cospectra to the Kaimel et al. (1972) model for the (top) 1–2 and (bottom) 3–4 axes. The observed variance-preserving cospectra from all depths were normalized by the model-estimated Reynolds stress and grouped into bins by wavenumber, normalized by the model-estimated roll-off wavenumber k_o. The median value (circle) and 2 times the bootstrapped standard error, utilized to reduce the effect of spectra noise, are shown for each wavenumber bin. The theoretical variance-preserving model cospectra (Fig. 4) is shown for comparison.

The mean uncertainty (Fig. 9, black circles) increased with increasing stress from 0.09 Pa at near-zero stress to 0.25 Pa at stresses of 0.5 Pa. For each direction, the mean stresses became larger than the mean uncertainty at magnitudes greater than 0.12–0.15 Pa ($\overline{u'w'} = 1.2 \times 10^{-4}$ to 1.5×10^{-4} m^2 s^{-2}). These uncertainty estimates were similar in magnitude to those reported for the variance method for mode-1 sampling (Lu and Lueck 1999; Williams and Simpson 2004).

6. CF-method results

a. Near-boundary stress comparisons

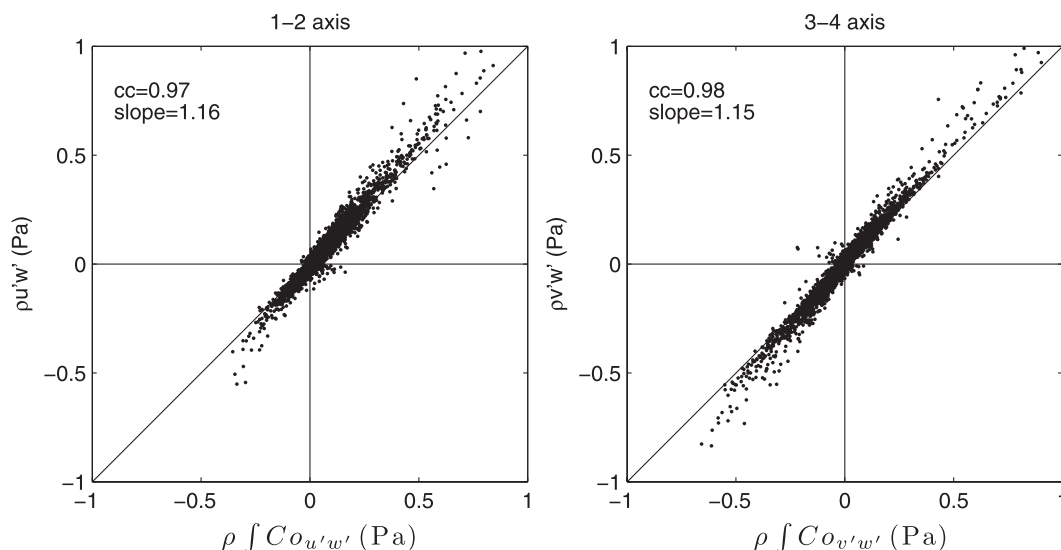Near-bottom stresses computed with the CF method were much closer to the expected bottom stress than

FIG. 8. Comparison of model (vertical axis) and observed (horizontal axis; the integral of the cospectrum from 0 frequency to the wave band cutoff) estimates of the Reynolds stresses. CC (the model skill) and linear regression slopes are shown for each axis: (left) 1–2 and (right) 3–4 axes.

stresses computed using the AF method (shown in section 4). Correlation coefficients between time series of CF-method stress in the first bin (3.3 m above the bottom) and the quadratic drag law ($\mathbf{U}|\mathbf{U}|$), calculated from the horizontal 1–2 and 3–4 velocities in bin 1, were 0.36 for the 1–2 direction and 0.68 for the 3–4 direction. Both were significantly different from zero at the 95% confidence level, which was found using the effective degrees of freedom (Chelton 1983). Bin averages of the CF-method stresses show a strong correspondence to the drag law along both axes (Figs. 10c,d, squares), in contrast to that shown for the AF method (Fig. 3). Without the wave–drift velocity criterion applied (Figs. 10c,d, triangles), estimated CF-method stresses were similar to the results using both criteria (Figs. 10c,d, squares), except at low values of the drag law. This difference suggests that the wave/drift velocity criterion has the most impact at low velocities or low stresses.

The slope of a linear regression between the CF-method near-bottom stress and ($\mathbf{U}|\mathbf{U}|$) gives an estimate of the quadratic drag coefficient C_d in each direction. Regressions between the burst time series yielded drag coefficients of 1.8×10^{-3} and 1.5×10^{-3} at 3.3 m above the bottom for the 1–2 and 3–4 axes, respectively. These values were similar to recent ADV-based stress estimates of $C_d = 3.4 \times 10^{-3}$ made near the MVCO site at 0.7 m above the bottom (J. Trowbridge 2009, personal communication), because drag coefficients would decrease with increasing height between 0.7 m and the 3.3-m height used here. The correspondence of the estimated drag coefficients, coupled with the positive

correlations between the stresses and the drag law, particularly in the 3–4 direction, suggest that the CF method was able to minimize the wave-induced stress errors and provide realistic estimates of near-bottom Reynolds stress.

Near-surface CF-method "ocean" stress estimates also compared well with estimates of wind stress from the nearby ASIT. In the surface-most bin, at 1.5-m depth, CF-method stress was positively correlated with the ASIT wind stress, with correlation coefficients of 0.84 and 0.52 for the 1–2 and 3–4 axes. Regression coefficients between the wind stress and ADCP-based stress at this depth, 1.11 ± 0.09 and 1.14 ± 0.21 for the 1–2 and 3–4 axes, were statistically indistinguishable from 1. At a depth of 3.0 m, CF-method stresses were also positively correlated with the local wind stresses, with correlation coefficients of 0.81 and 0.74 for the 1–2 and 3–4 axes. Regression coefficients for 3.0-m depth were reduced relative to those found at 1.5 m, at 0.72 ± 0.06 and 0.75 ± 0.07 for the 1–2 and 3–4 axes, which is consistent with a reduction of the surface boundary stress with depth.

Bin averages of these near-surface CF-method stress estimates illustrate the strong correspondence between the near-surface stresses and the local wind stress (Figs. 10a,b). The largest deviations from the wind stress are seen along the 3–4 axis at 1.5-m depth for near-zero or negative wind stresses corresponding to a regression intercept of -0.075 Pa. Because the intercept is near zero at 3.0-m depth along this axis, it is unclear what causes the bias at 1.5-m depth. Along the 1–2 axis, regressions at both
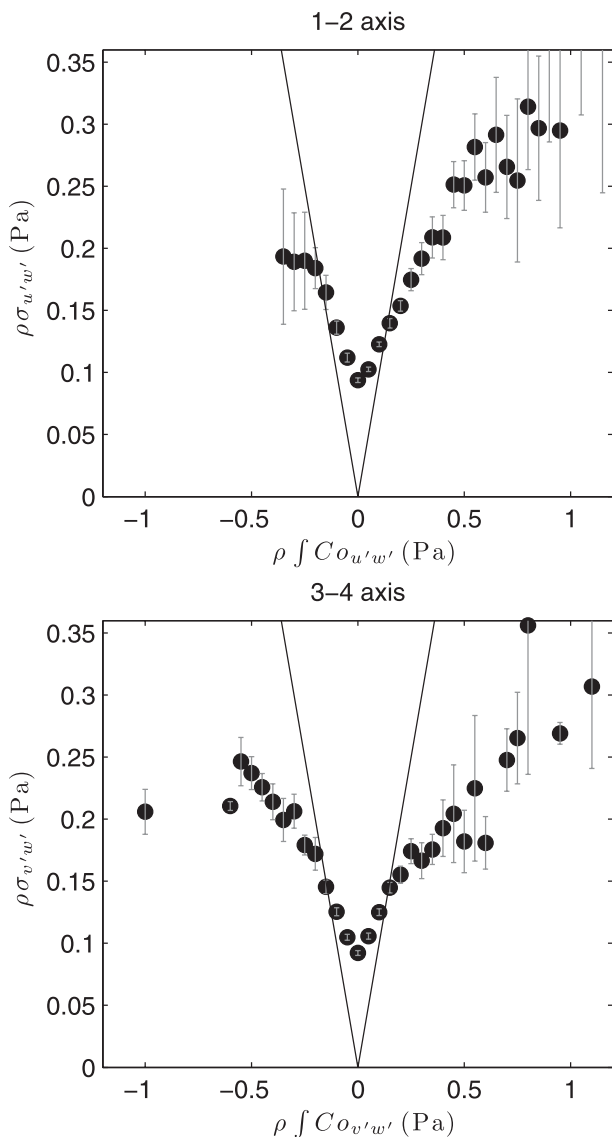
FIG. 9. Bin-averaged (top) 1–2 and (bottom) 3–4 axes cospectral uncertainty estimates (defined here as the standard deviation of the error histogram) for the CF method, plotted against the integrated below–wave band cospectra, the below–wave band covariance. Standard error bars, estimated using the independent degrees of freedom (Chelton 1983), are shown for each bin average. Thin lines mark where the stress level becomes larger than the mean uncertainty estimate.

depths appear to have a mean offset of −0.025 Pa that was similar in magnitude to the mean offset for the near-bottom regression (Fig. 10c). ASIT wind stresses were used for these comparisons, rather than the longer record existing at the Shore Meteorological Station (Fig. 2), to better match conditions present offshore at the 12-m node. Similar correlations existed between the near-surface CF-method stresses and shore-based winds for

the entire study period, although the magnitudes of the shore-based wind stresses were smaller, leading to larger regression coefficients.

b. Tidal stress vertical profiles

Tidal dynamics provide a good test of the ability of the CF method to measure the vertical structure of stress. Because the majority of the tidal flow occurred along the 3–4 axis at MVCO, we focus on the dominant M_2 component of stress along this axis to find the vertical structure of tidal stresses estimated using the CF method. The M_2 component of the 3–4 axis stress was isolated for all depth bins using T_tide (Pawlowicz et al. 2002) and averaged into 30° phase blocks (Fig. 11). For all phases, the tidal stress generally increased with increasing depth, with maximum stresses increasing from 0.3×10^{-4} m^2 s^{-2} near the surface to greater than 0.75×10^{-4} m^2 s^{-2} at 4.1 m above the bottom when $\theta = 45°$ and $255°$, maximum along-axis ebb or flood. Slack-water tidal stresses ($\theta = 135°$ and $315°$) were nearly uniform with depth and generally less than 0.1×10^{-4} m^2 s^{-2} near the surface and 0.2×10^{-4} m^2 s^{-2} near the bottom. These results are similar to previous ADCP-based studies of tidal channel stresses using the variance method (Rippeth et al. 2003; Williams and Simpson 2004).

An evaluation of the observed M_2 tidal stresses can be made by comparing the structure seen in Fig. 11 to tidal stress profiles inferred from a simple momentum balance. To predict of the vertical structure of tidal stress along the 3–4 axis, we integrate the linear, along-axis momentum equation,

$$\frac{\partial V}{\partial t} + fU = -\frac{1}{\rho}\frac{\partial P}{\partial y} + \frac{\partial}{\partial z}\frac{\tau^y}{\rho}, \qquad (19)$$

where t is time; f is the Coriolis parameter; ρ is a reference density; and τ^y is the tidal stress, from the surface to each depth z:

$$\int_z^0 \frac{\partial v}{\partial t}\,dz + \int_z^0 fu\,dz = -\frac{z}{\rho}\frac{\partial P}{\partial y} + \frac{\tau^y}{\rho}, \qquad (20)$$

assuming a barotropic along-axis pressure gradient and $\tau^y = 0$ at the surface. Thus, a prediction of the vertical structure of τ^y can be made using the sum of the first three terms of (20), given estimates of M_2 tidal velocities and the along-axis pressure gradient. M_2 tidal velocities were estimated from the burst-mean velocities $[\mathbf{U}(z, t)]$ using T_tide (Pawlowicz et al. 2002) and were similarly phase averaged. The barotropic pressure gradient was estimated by evaluating (20) at 4 m above the bottom, using
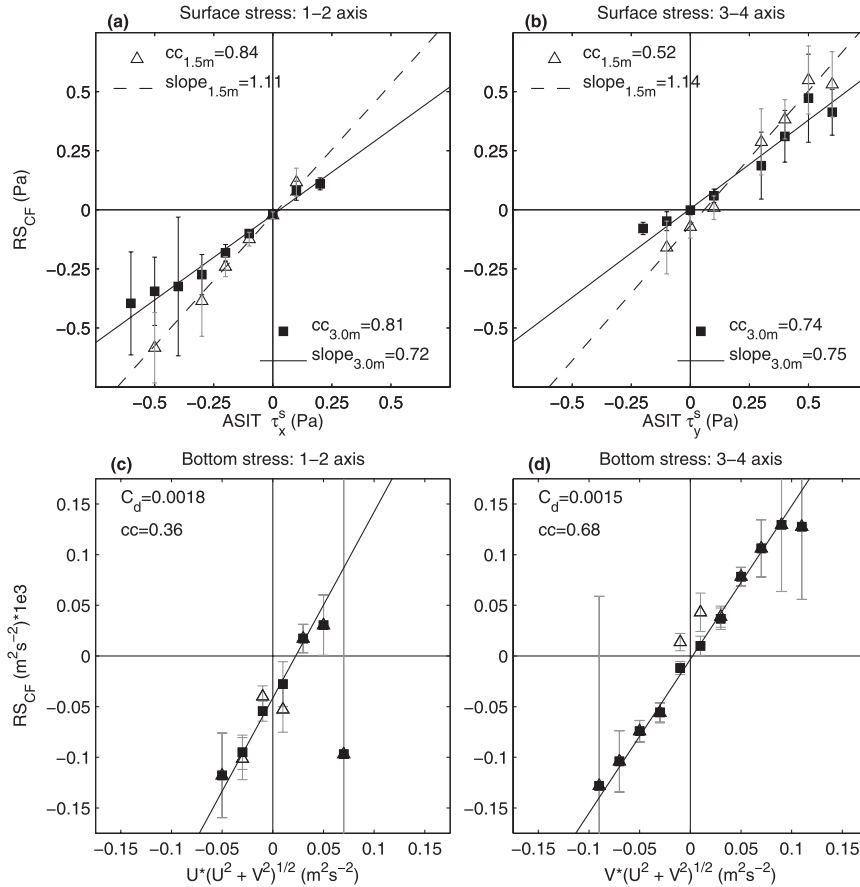
FIG. 10. Bin-averaged comparisons of (top) CF-method Reynolds stresses at 1.5 and 5 m below the surface to wind stresses from MVCO's nearby ASIT (days 17–30 only) and (bottom) CF-method Reynolds stresses 3.3 m above the bottom to the quadratic drag law, calculated using burst-mean velocities from the bottommost ADCP bin. For the (left) 1–2 and (right) 3–4 axes, bin-averaged stresses are shown for k_o bounded bursts (triangles) and bursts meeting both screening criteria (squares). Standard error bounds, estimated using the effective degrees of freedom (Chelton 1983), are given for each bin. Linear regressions, slopes C_d, and CC between the raw (not bin-averaged) time series of the screened stress results are shown.

the observed phase-averaged stress at that depth. This prediction of the tidal stress using the momentum balance allows an evaluation of the vertical structure of the ADCP-based stress profiles relative to the anchor point.

The vertical structure of this sum was similar to the vertical structure of the observed tidal stress at all depths and all phases, often within the standard error bounds of the observations (Fig. 11). The predicted stress was slightly larger than the observed stresses between 5 and 6 m above the bottom for many of the phase averages, perhaps because the anchor point used (4 m) was often the maximum stress seen. However, a strong correspondence between predicted and observed stresses exists at the top of the measured portion of the water column. That these profiles were similar far from

the anchor point suggests that the CF method captured the vertical structure of tidal stress well.

c. Turbulence length scales

The roll-off wavenumbers estimated as part of the model fit to the below–wave band cospectra represent the horizontal length scales of the dominant stress-carrying eddies. Along both axes, roll-off wavenumbers, k_o, corresponded to roll-off wavelengths ($\lambda_o = 2\pi/k_o$) that were generally larger than the vertical distance to the boundary, and often larger than the water column depth. For the 3–4 axis, median values of λ_o (shown as $\lambda_o/10$ in Fig. 12) for each depth bin increased from 12 m near the bed to 21 m in the middle of the water column. For the 1–2 axis, λ_o was less variable with depth, increasing from 13 m near the bed to 18 m in the middle of the water column.
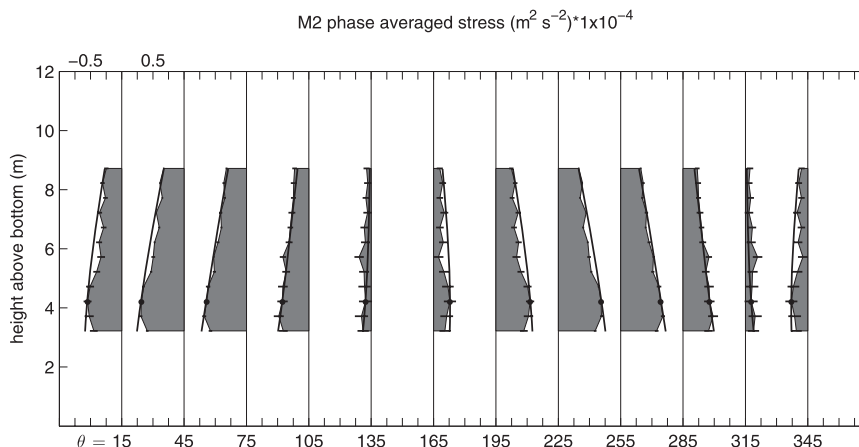
M2 phase averaged stress (m² s⁻²)*1x10⁻⁴

FIG. 11. Observed 3–4 axis stresses associated with the M_2 tidal frequency, isolated using T_tide (Pawlowicz et al. 2002) and averaged into 30° phase blocks (shaded profiles with standard deviations shown) compared to the predicted stress (solid line) based on (20). The dot in each profile at 4.1 m above the bottom marks the depth to which (20) was solved explicitly to estimate the along-axis barotropic pressure gradient. Tick marks are 0.25×10^{-4} m² s⁻², and each profile is offset by 1×10^{-4} m² s⁻² with the corresponding phase angle θ given below.

These horizontal length scales can be compared to more familiar vertical length scales of oceanic turbulence. Given the unstratified conditions present in January at MVCO, the "mixing length scale" discussed by Dillon (1982)—written here for the 1–2 axis as

$$l_m = \left(\frac{\overline{-u'w'}}{S^2} \right)^{1/2}, \qquad (21)$$

where S is the burst-mean shear $\partial U/\partial z$—is representative of a vertical length scale of turbulent mixing. Calculated using the model-estimated stress and observed shear, estimates of l_m increased from 1.5 to 1.75 m for the 1–2 axis and from 0.5 to 1.25 m for the 3–4 axis (Fig. 12). In both directions, l_m exhibited a similar vertical structure as the corresponding roll-off wavelengths, despite being an order of magnitude smaller.

These similarities in vertical structure suggest a correspondence between these horizontal and vertical estimates of the turbulent length scales. Together, they give an indication of the anisotropy of the dominant stress-carrying eddies (roughly a factor of 10–15 here) that cause mixing. Using ADCP-based stress estimates in a tidal channel, Stacey et al. (1999a) made a similar comparison between the mixing length scale l_m and an integral length scale of the stress, based on autocorrelation functions of the along-beam velocities. Stacey et al. (1999a) found this horizontal scale (3–10 m) to be 5–6 times larger than the vertical scale l_m, both of which were similar to previous estimates for estuarine tidal boundary layers by Gross and Nowell (1982).

7. Tilt bias evaluation

As shown by (8) and (9), a small tilt of the ADCP relative to the coordinate system of interest can induce large errors in the estimated stresses. Previously, the magnitude of these errors were estimated solely via scaling arguments (Lu and Lueck 1999; Williams and Simpson 2004; Rosman
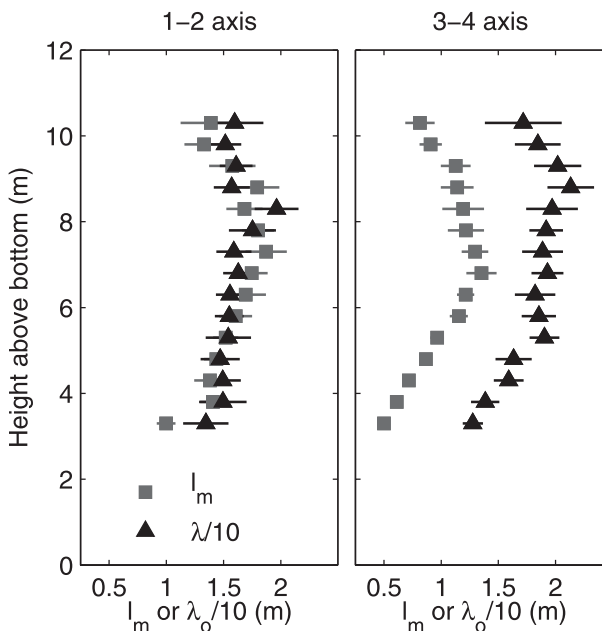

FIG. 12. Median profiles (with bootstrapped standard error) of the vertical mixing length scale l_m and the horizontal roll-off wavelength $\lambda_o = 2\pi/k_o$ for the (left) 1–2 and (right) 3–4 axes.

et al. 2008), which, for the pitch and roll measured by the MVCO ADCP ($P = -2.3°$ and $R = 3.3°$), would predict tilt-related biases that can approach half of the magnitude of the stresses themselves along both axes. However, such sizable additions to the CF-method estimated stresses are not seen in comparisons between near-boundary stresses and the bottom drag law or wind stress. Regression intercepts—the mean bias—were near zero for the 3–4 axes (except at 1.5-m depth) and -0.025 to -0.04 Pa for the 1–2 axis (Fig. 10). Because efforts to minimize these tilt errors drive the deployment requirements of ADCPs measuring stresses and limit the usefulness of previously collected measurements with significant tilts, it is worthwhile to understand the differences seen between scaling arguments and the observations.

The large sizes of the stress-carrying turbulent eddies (estimated from k_0 in the model fits) allow quantitative assessment of tilt-related errors. At 3.3 m above the bottom in bin 1, horizontal length scales ($\lambda_0 = 2\pi k_0$) are 6–15 m, much larger than the horizontal separation of the beams at this depth (0.78 m). Thus, transforming the beam coordinate velocities (u_1, u_2, u_3, and u_4) to instrument-coordinate velocities (u_I, v_I, and w_I) results in a "point measurement" of velocity that still resolves the dominant stress-carrying turbulent eddies. Consistent with this supposition, stresses estimated directly from this point measurement of velocity using the instrument-coordinate cospectra and the CF method ($\overline{u_I'w_I'}, \overline{v_I'w_I'}$) were virtually identical to stress estimates derived directly from the along-beam velocities using (14) and (15) (comparison not shown).

Because the bin-1 stress estimates from point velocities were consistent with those from the along-beam estimates, an additional step was taken to examine the tilt-biases in the along-beam stress estimates. Earth coordinate Reynolds stresses [RS$_{earth}$; term 2 in (8) and (9)] were found by applying the CF method to cospectra of the earth coordinate velocities (u, v, w) formed by rotating (u_I, v_I, w_I) to account for the measured pitch and roll of the instrument. Likewise, terms 3 and 4 in (8) and (9) were estimated from (u, v, w) using the CF method. Comparisons of the error terms in (8) and (9) to the along-beam stress estimates from (14) and (15) (denoted as RS$_{beam}$) reveals that the true errors resulting from instrument tilt were less than the theoretical maximum possible for these tilts, the anisotropic limit (Fig. 13). Based on linear regressions between time series of each term in (8) and (9), the tilt-related errors (terms 3 and 4) averaged 32% and 5% of RS$_{beam}$ (term 1) for the 1–2 axis and 21% and 5% of RS$_{beam}$ for the 3–4 axis (Fig. 13). In contrast, assuming a moderate amount of anisotropy following Lu and Lueck (1999), theoretical estimates of the term-3 error, $5\overline{u'w'}\phi_r$ and $5\overline{v'w'}\phi_p$,

predict slopes that are similar to those observed (Fig. 13). However, these estimates do not account for the mean term-3 error (the regression intercept), which, at 1.0×10^{-4} and 0.5×10^{-4} m^2 s^{-2} for the 1–2 and 3–4 axes, respectively, is the dominant source of tilt-related stress error for small to moderate stresses.

The near-bottom estimates of RS$_{earth}$ were highly correlated with RS$_{beam}$ and had similar correlation magnitudes with the quadratic drag law (Table 1). Linear regressions between RS$_{earth}$ and $\mathbf{U}|\mathbf{U}|$ gave slopes (drag coefficients) that were slightly less than those found for RS$_{beam}$ and intercepts that were more positive but closer to zero only for the 1–2 axis (Table 1). The differences between the regression intercepts of RS$_{beam}$ and RS$_{earth}$ versus $\mathbf{U}|\mathbf{U}|$ were similar to the mean of terms 3 and 4 (Table 1). However, the regressions between RS$_{earth}$ and the quadratic drag law were still offset from zero for both axes (Fig. 14, triangles), meaning that an additional bias still exists in these "true" stress estimates. Possible explanations for this additional stress bias include potential flow around the bottom lander or errors in the pitch and roll measurements themselves.

To account for this additional offset, an independent estimate of the tilt of the instrument relative to the flow ($P = -0.3°$ and $R = 2°$ with estimated standard deviations of 0.8° and 1.3°, respectively) was found by minimizing the standard deviation of the burst-mean, earth coordinate vertical velocity for the 30-day time series. Using these smaller tilt angles, error terms in (8) and (9) had reduced magnitudes relative to RS$_{beam}$ and regressions of the new earth coordinate Reynolds stresses (RS$_{earth–fit}$) had near-zero intercepts. Linear regressions between time series of each term in (8) and (9) finds the two tilt error terms (terms 3 and 4) averaged 14% and <1% of RS$_{beam}$ for the 1–2 axis and 2% and 3% of RS$_{beam}$ for the 3–4 axis (Fig. 13). Stress offsets for RS$_{earth–fit}$ are near zero (Fig. 14). The differences between RS$_{beam}$ and RS$_{earth–fit}$ intercepts were also consistent with the magnitude of the mean error likely because of instrument tilt, particularly along the 3–4 axis (Table 1).

8. Discussion

It is important to understand why the AF method gave stress estimates that were significantly correlated with a near-bottom quadratic drag law for the datasets used by Rosman et al. (2008) but was unable to do so here where the CF method performed well. Because application of the CF method was limited by the threshold criteria, it is possible that the limiting criteria themselves caused the differing results and that viable stress estimates are not possible during these excluded times for
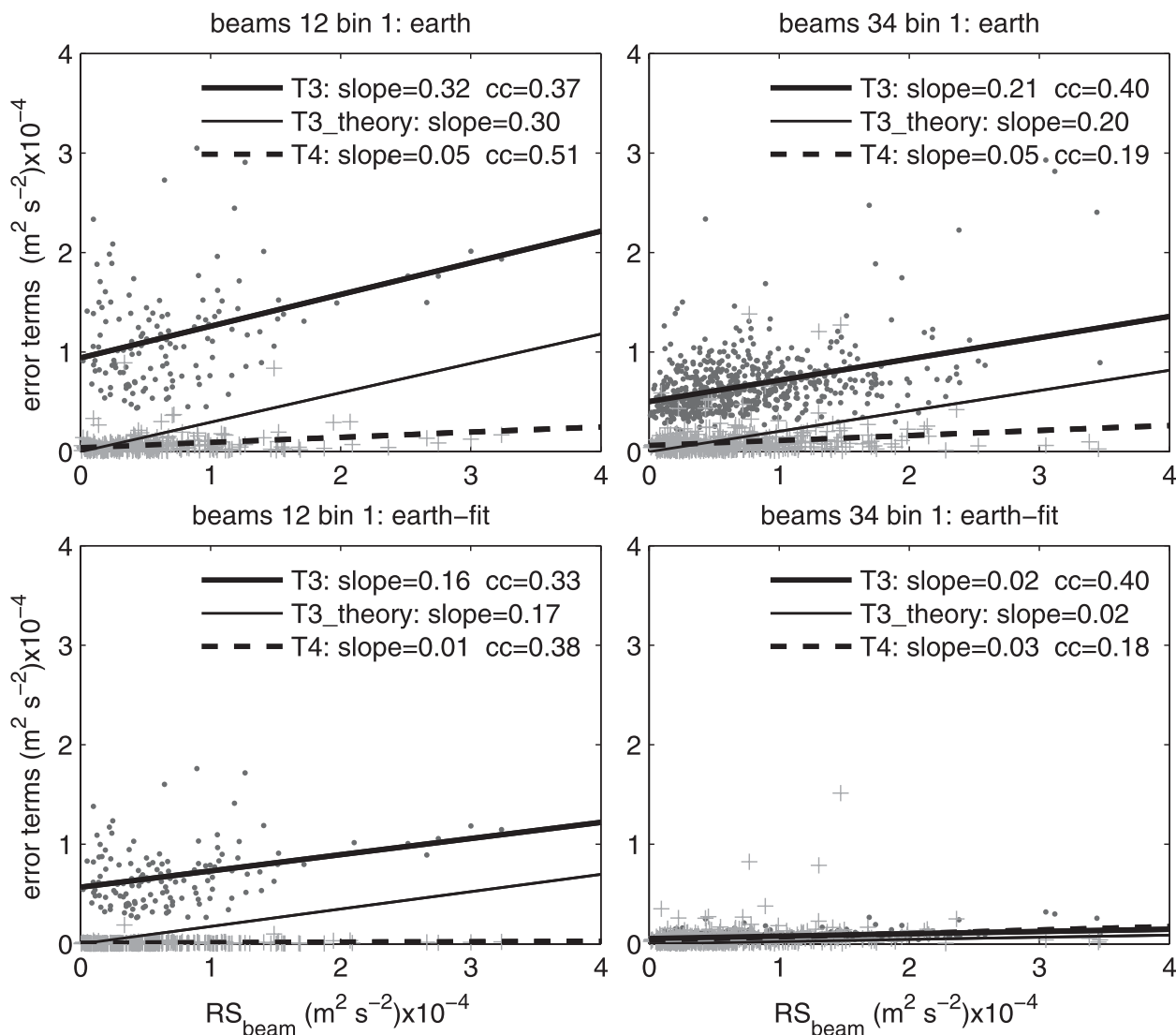
FIG. 13. The (left) 12 and (right) 34 axes bin-1 estimates of earth coordinate stress error terms 3 (dots) and 4 (crosses) in (8) and (9) vs the beam-coordinate stress RS_{beam} using (top) the measured instrument tilt values (earth) and (bottom) tilt estimates from minimizing the standard deviation of the burst vertical velocity (earth fit). Linear regressions, slopes, and CC between errors and the measured stress (term 3: thick solid lines; term 4: dashed lines) are shown, as well as theoretical estimates for term 3 ($5\overline{u'w'}\phi_r$, $5\overline{v'w'}\phi_p$) following Lu and Lueck (1999).

either method. Limiting the examination of near-bottom AF-method stresses (Fig. 3) to only those bursts that passed both threshold criteria used in the CF method only (squares) slightly improves the correlation coefficients (CC = 0.06 and 0.24 for the 1–2 and 3–4 axes). For this second comparison, regression slopes (drag coefficients) were much smaller than for the CF method, at 0.3×10^{-3} and 0.5×10^{-3} for the 1–2 and 3–4 axes, with significant scatter (Fig. 3). Although the correlation for the 3–4 axis is now stronger, the AF method still performs poorly during these times in comparison to the CF method (Fig. 10).

An analysis of the performance of the AF and CF methods for the sample burst shown in Fig. 5 suggests how and why the AF method might be failing. Within the wave band frequencies $0.45 \leq \omega \leq 2$ rad s^{-1}, raw along-beam velocity spectra ($S_{u_3 u_3}$ and $S_{u_4 u_4}$ in Fig. 5a) are 20 times larger than those outside. Thus, the cospectrum, calculated following (15), has large negative values in this band that are likely due to waves and not turbulence (Fig. 5b). These large values would significantly bias a Reynolds stress estimated from the total covariance (the integral of the observed cospectrum) following the variance method alone. Applying the AF

TABLE 1. Regression results for CF-method bin-1 stress estimates and the quadratic bottom drag $\mathbf{U}|\mathbf{U}|$ along with mean tilt errors, the sums of terms 3 and 4 in (8) and (9).

Beam axis	Stress source	Correlation coef	Slope (C_d) ($\times 10^{-3}$)	Intercept offset (10^{-5} m^2 s^{-2})	Mean tilt error (10^{-5} m^2 s^{-2})
12	RS_{beam}	0.36	1.8	−4.1	—
	RS_{earth}	0.54	2.0	1.1	11.5
	$RS_{earth–fit}$	0.51	1.8	−0.6	6.8
34	RS_{beam}	0.68	1.5	−0.3	—
	RS_{earth}	0.70	1.5	2.6	6.3
	$RS_{earth–fit}$	0.64	1.3	−0.1	0.6

method to this burst greatly reduces the cospectral energy present in the wave band but leaves small negative values at these frequencies (Fig. 5b). As illustrated by the Ogive curve of the AF-method cospectrum (Fig. 5c, gray curve), the residual errors in this example act to decrease the integrated cospectrum within the wave band such that the total covariance, the high-frequency end point of the curve, is near zero. In contrast, the model fit used in the CF method (Fig. 5c, dashed curve) predicts a total covariance near 1×10^{-4} m^2 s^{-2} (Fig. 5c).

The contrasting results of the CF and AF method shown for this burst are representative for bursts of this dataset having successful CF-method stress estimates. Given the variable performance of the AF method here, within the two datasets used by Rosman et al. (2008) obtained under more moderate wave conditions, as well as the failures described by Feddersen and Williams

(2007) for the ADV-based observations, it is clear that the method breaks down as waves become more broad banded in frequency and larger in amplitude. As illustrated by this burst and Figs. 7, 8, 10, and 11, the model used in the CF method matches the below–wave band cospectral observations well, giving stress estimates that were similar to the below–wave band integrals of the cospectra (the below–wave band covariance) and were reasonable throughout the water column. However, given the CF-method limitations described later, additional analysis of both methods is needed to determine the exact parameter ranges where performance of each is optimized.

Although the CF method provides a successful way to eliminate the wave-induced stress bias, application of the method is limited by a number of factors. The screening criteria used ($k_o < k_{wc}$ and $\sigma_w/U_d < 2$) limit
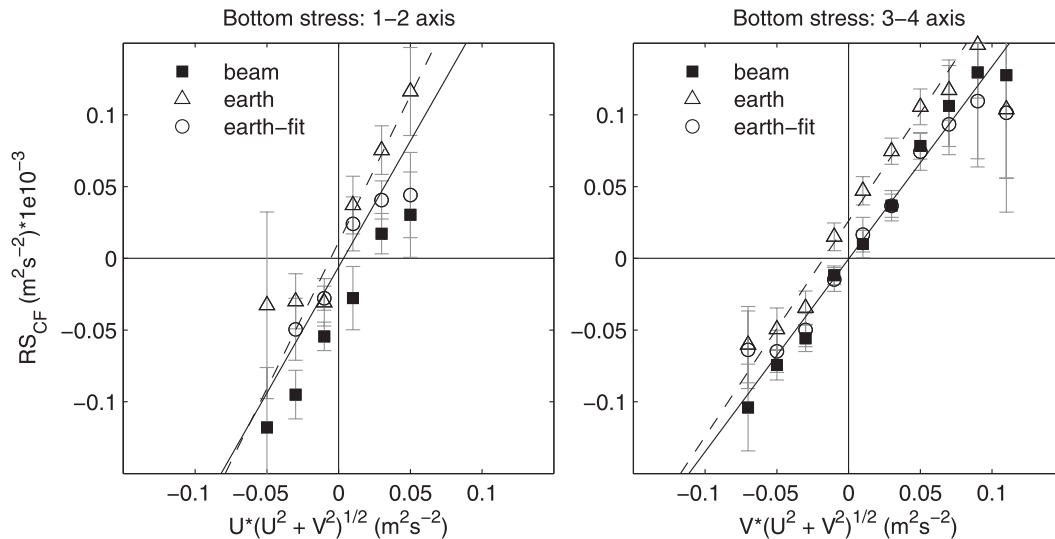

FIG. 14. Correcting the tilt bias in near-bottom stress estimates. Bin-averaged comparisons of beam-coordinate-based CF-method stresses 3.3 m above the bottom and the quadratic bottom drag law (beam; from Fig. 10) are shown with similar comparisons between earth coordinate–based CF-method Reynolds stresses, using two estimates of the instrument tilt (earth and earth fit) and the quadratic bottom drag law. Standard error bounds, using independent degrees of freedom, are given for each bin average. Linear regressions between the raw time series of earth coordinate stresses (earth: dashed line; earth fit: solid line) and quadratic bottom drag are shown with drag coefficients (slopes) and y intercepts (mean offsets) given in Table 1: (left) 1–2 and (right) 3–4 axes.

the amount of valid stress measurements to 40% of the total bursts, rejecting bursts with shorter turbulent length scales and those with weaker mean flows and/or stronger waves. As a result, the method is unable to make stress estimates in these conditions, potentially biasing mean stress results toward those found in stronger mean flow, smaller wave conditions. However, it is important to note the potential bias to longer turbulent length scales is partially consistent with the vertical bin size bias of the instrument itself (Stacey et al. 1999a), both of which can limit the application of this method in environmental flows with shorter turbulent length scales (e.g., stronger stratification). Additionally, considerable noise exists in the individual cospectra; thus applying the k_o criteria a posteriori could allow bursts with ''good'' model fits to be cut and bursts with questionable model fits to be kept if the true k_o differs greatly from the estimated k_o. Although the stress uncertainty resulting from cospectral noise was assessed with the error estimates, the effect of error in this criterion has not been assessed.

The nonparametric approach used to calculate uncertainties for the covariance found a noise floor of 0.1 Pa and uncertainties of 50% using RDI mode 1 (Fig. 9), similar to that found for the variance method (Lu and Lueck 1999; Williams and Simpson 2004). Averaging reduced the uncertainty values significantly, with relative errors approaching 0.01 Pa or 1×10^5 m^2 s^2 for the tidal stress comparison (Fig. 11), and individual stress estimates appeared reasonable at levels below the estimated uncertainties. This suggests that the methodology used here to estimate uncertainty may be in need of improvement, perhaps through the development of a theoretical framework similar to Williams and Simpson (2004) or revisiting the nonparametric approach utilized. Applying the Monte Carlo–type method used here also proved to be computationally expensive, accounting for more than 80% of the computing time required for each burst. Additionally, the covariance uncertainties do not account for stress errors resulting from the limitations of the instrument or CF method described earlier.

Thus, a number important questions remain regarding the differences between the AF and CF methods and the application of the CF method. Although work to directly compare AF- and CF-method results under a broad range of wave conditions is currently underway, detailed comparisons of ADCP-based CF-method stresses to lower-noise, turbulence-specific measurements are needed to revisit the uncertainty estimates and assess the role of instrument-specific limitations on the CF-method stress estimates. Such work would be able to define the parameter range (i.e., wave climates, current speeds, stratification levels, and stress magnitudes) in which

ADCP-based stress estimates can be accurately made using the CF method. Additionally, because the mean stress bias resulting from nonzero instrument tilt appears to account for the bulk of the total tilt-related bias, the offset between these bin-1 regressions could serve as a tilt-bias correction for RS$_{bc}$ stress estimates at all depths. This correction, potentially allowing viable stress observations from large-tilt deployments, needs further investigation.

9. Conclusions

The variance-method framework for estimating stresses from ADCP observations could be an invaluable tool for understanding coastal ocean dynamics. However, previous methods to eliminate biases resulting from wave orbital velocities in stress estimates (Whipple et al. 2006; Rosman et al. 2008) proved inadequate using the test dataset. In contrast, the cospectra-fit (CF) method described here and in Gerbi et al. (2008) provided an accurate way to calculate Reynolds stresses from ADCP observations in the presence of surface gravity waves. The method works by fitting an established semiempirical model of boundary layer turbulence to the measured turbulent cospectra at frequencies below those of surface gravity waves to estimate the stress. With only the below–wave band cospectrum used to estimate stresses, the residual wave biases existing in previous techniques were not seen.

Applying the CF method to observations made in weakly stratified waters 12 m deep, near-surface stresses were positively correlated (CC = 0.52 and 0.84) and close in magnitude (regression slopes = 1.14 and 1.11) with estimates of local wind stress along both measurement axes. Near-bottom stress estimates were similarly correlated (CC = 0.68 and 0.36) with the estimated quadratic bottom drag, providing drag coefficients (C$_d$ = 1.5×10^{-3} to 1.8×10^{-3} at 3.3 m above the bottom) consistent with previous independent estimates for the study area. Additionally, the vertical structure of stress along the 3–4 axis, filtered to isolate the M_2 tide, matched that inferred from a linear momentum balance forced by a barotropic pressure gradient. Within the bursts passing two limiting criteria of the CF method, as much as 83% of the total turbulent stresses existed at frequencies below those of surface gravity waves.

The roll-off wavenumbers k_o, estimated as part of the CF-method model fit, provide estimates of the horizontal length scales of the dominant stress-carrying turbulent eddies. Combined with estimates of vertical mixing length scales, they describe the three-dimensional size of the turbulent scales present. Because these length scales were large for the test dataset (averaging 12–18 m), the

stress errors resulting from instrument tilt could be directly calculated in the bottommost bin where beam separation is small. Tilt-related errors were similar to theoretical estimates based on scaling arguments that assumed moderate anisotropy and served as a useful diagnostic of the instrument's tilt relative to the flow field.

REFERENCES

Chelton, D., 1983: Effects of sampling errors in statistical estimation. *Deep-Sea Res.,* **30,** 1083–1101.

Dillon, T., 1982: Vertical overturns: A comparison of Thorpe and Ozmidov length scales. *J. Geophys. Res.,* **87,** 9601–9613.

Feddersen, F., and A. Williams, 2007: Direct estimation of the Reynolds stress vertical structure in the nearshore. *J. Atmos. Oceanic Technol.,* **24,** 102–116.

Garvine, R., 2004: The vertical structure and subtidal dynamics of the inner shelf off New Jersey. *J. Mar. Res.,* **62,** 337–371.

Gerbi, G., J. Trowbridge, J. Edson, A. Plueddemann, E. Terray, and J. Fredericks, 2008: Measurements of momentum and heat transfer across the air–sea interface. *J. Phys. Oceanogr.,* **38,** 1054–1072.

Gross, T., and A. Nowell, 1982: Mean flow and turbulence scaling in a tidal boundary layer. *Cont. Shelf Res.,* **2** (2–3), 109–126.

Kaimel, J. C., J. C. Wyngaard, Y. Izumi, and O. Coté, 1972: Spectral characteristics of surface-layer turbulence. *Quart. J. Roy. Meteor. Soc.,* **98,** 563–589.

Large, W., and S. Pond, 1981: Open ocean momentum flux measurements in moderate to strong winds. *J. Phys. Oceanogr.,* **11,** 324–336.

Lentz, S., 1994: Current dynamics over the northern California inner shelf. *J. Phys. Oceanogr.,* **24,** 2461–2478.

Lohrmann, A., B. Hackett, and L. Roed, 1990: High-resolution measurements of turbulence, velocity, and stress using a pulse-to-pulse coherent sonar. *J. Atmos. Oceanic Technol.,* **7,** 19–37.

Lu, Y., and R. Lueck, 1999: Using a broadband ADCP in a tidal channel. Part II: Turbulence. *J. Atmos. Oceanic Technol.,* **16,** 1568–1579.

Lumley, J., and E. Terray, 1983: Kinematics of turbulence convected by a random wave field. *J. Phys. Oceanogr.,* **13,** 2000–2007.

Munchow, A., and R. Chant, 2000: Kinematics of inner shelf motions during the summer stratified season off New Jersey. *J. Phys. Oceanogr.,* **30,** 247–268.

Nidzieko, N., D. Fong, and J. Hench, 2006: Comparison of Reynolds stress estimates derived from standard and fast-ping ADCPs. *J. Atmos. Oceanic Technol.,* **23,** 854–861.

Pawlowicz, R., B. Beardsley, and S. Lentz, 2002: Classical tidal harmonic analysis including error estimates in MATLAB using T_TIDE. *Comput. Geosci.,* **28,** 929–937.

Rippeth, T., E. Williams, and J. Simpson, 2002: Reynolds stress and turbulent energy production in a tidal channel. *J. Phys. Oceanogr.,* **32,** 1242–1251.

——, J. Simpson, and E. Williams, 2003: Measurement of the rates of production and dissipation of turbulent kinetic energy in an energetic tidal flow: Red Wharf Bay revisited. *J. Phys. Oceanogr.,* **33,** 1889–1901.

Rosman, R., J. Hench, J. Koseff, and S. Monismith, 2008: Extracting Reynolds stresses from acoustic Doppler current profiler measurements in wave-dominated environments. *J. Atmos. Oceanic Technol.,* **25,** 286–306.

Shaw, W., and J. Trowbridge, 2001: The direct estimation of near-bottom turbulent fluxes in the presence of energetic wave motions. *J. Atmos. Oceanic Technol.,* **18,** 1540–1557.

Stacey, M., S. Monismith, and J. Burau, 1999a: Measurements of Reynolds stress profiles in unstratified tidal flow. *J. Geophys. Res.,* **104** (C5), 10 933–10 949.

——, ——, and ——, 1999b: Observations of turbulence in a partially stratified estuary. *J. Phys. Oceanogr.,* **29,** 1950–1970.

Trowbridge, J., 1998: On a technique for measurement of turbulent shear stress in the presence of surface waves. *J. Atmos. Oceanic Technol.,* **15,** 290–298.

——, and S. Elgar, 2001: Turbulence measurements in the surf zone. *J. Phys. Oceanogr.,* **31,** 2403–2417.

——, and ——, 2003: Spatial scales of stress-carrying nearshore turbulence. *J. Phys. Oceanogr.,* **33,** 1122–1128.

Warner, J., C. Sherwood, H. Arango, and R. Signell, 2005: Performance of four turbulence closure models implemented using a generic length scale method. *Ocean Modell.,* **8,** 81–113.

Whipple, A. C., R. A. Luettich Jr., and H. E. Seim, 2006: Measurements of Reynolds stress in a wind-driven lagoonal estuary. *Ocean Dyn.,* **21,** 169–185, doi:10.1007/s10236-005-0038-x.

Williams, E., and J. Simpson, 2004: Uncertainties in estimates of Reynolds stress and TKE production rate using the ADCP variance method. *J. Atmos. Oceanic Technol.,* **21,** 347–357.